Roles of inter-leaflet coupling and hydrophobic mismatch in lipid membrane phase-separation kinetics – Supporting Information.

Philip W. Fowler[1,†], John. J. Williamson[2,‡], Mark S. P. Sansom[1], and Peter D. Olmsted[3,*]

[1]Department of Biochemistry, University of Oxford, South Parks Rd, Oxford, OX1 3QU, UK

[2]The Francis Crick Institute, Lincoln's Inn Fields Laboratories, 44 Lincoln's Inn Fields, London WC2A 3LY, UK

[3]Department of Physics, Institute for Soft Matter Synthesis and Metrology, Georgetown University, 37th and O Streets, N.W., Washington, D.C. 20057, USA

List of Tables

List of Figures

* To whom correspondence should be addressed. Email: pdo7@georgetown.edu.

† Current address: Nuffield Department of Medicine, John Radcliffe Hospital, University of Oxford, Headley Way, Oxford, OX3 9DU, UK

‡ Current address: The Francis Crick Institute, Lincoln's Inn Fields Laboratories, 44 Lincoln's Inn Fields, London WC2A 3LY, UK

Sim Id.	No. Lipids	Width (nm)	Unsat. no.	Saturated no.	Saturated lipid.	Chol. no.	Water	Na$^+$/Cl$^-$	Total Beads
3:0-6000-1	6,000	39.6	1,800	3,004	DLPC	1,196	81,008	2016	146,248
3:0-6000-2	6,000	39.8	1,800	3,004	DLPC	1,196	80,700	2016	145,940
3:0-6000-3	6,000	39.5	1,800	3,004	DLPC	1,196	80,824	2016	146,064
3:0-6000-4	6,000	40.8	1,800	3,004	DLPC	1,196	81,008	2016	146,248
4:0-6000-1	6,000	40.8	1,800	3,004	DPPC	1,196	65,984	2016	137,232
4:0-6000-2	6,000	40.7	1,800	3,004	DPPC	1,196	65,980	2016	137,228
4:0-6000-3	6,000	40.8	1,800	3,004	DPPC	1,196	66,092	2016	137,340
5:0-6000-1	6,000	39.6	1,800	3,004	DAPC	1,196	90,660	2016	167,916
5:0-6000-1	6,000	39.6	1,800	3,004	DAPC	1,196	90,660	2016	167,916
5:0-6000-1	6,000	39.6	1,800	3,004	DAPC	1,196	90,584	2016	167,840
3:0-3200-1	3,200	30.0	960	1,600	DLPC	640	18,208	720	52,288
3:0-1600-1	1,600	21.3	480	800	DLPC	320	14,896	420	32,056
3:0-800-1	800	14.9	240	400	DLPC	160	4,552	180	13,072
3:0-400-1	400	10.8	120	200	DLPC	80	3,724	105	8,014
3:0-200-1	200	7.5	60	100	DLPC	40	1,138	45	3,268
3:0-100-1	100	5.3	30	50	DLPC	20	578	23	1,646
4:0-3200-1	3,200	29.9	960	1,600	DPPC	640	18,208	720	55,488
4:0-1600-1	1,600	21.2	480	800	DPPC	320	14,896	420	33,656
4:0-800-1	800	15.0	240	400	DPPC	160	4,552	180	13,872
4:0-400-1	400	10.6	120	200	DPPC	80	3,724	105	8,414
4:0-200-1	200	7.6	60	100	DPPC	40	1,138	45	3,468
4:0-100-1	100	5.3	30	50	DPPC	20	578	23	1,748
5:0-3200-1	3,200	29.6	960	1,600	DAPC	640	18,208	720	58,688
5:0-1600-1	1,600	21.1	480	800	DAPC	320	14,896	420	35,256
5:0-800-1	800	14.9	240	400	DAPC	160	4,552	180	14,672
5:0-400-1	400	10.6	120	200	DAPC	80	3,724	105	8,814
5:0-200-1	200	7.5	60	100	DAPC	40	1,138	45	3,668
5:0-100-1	100	5.4	30	50	DAPC	20	578	23	1,850
5:0-2880-1	2,880	29.3	960	1,600	DAPC	320	18,208	720	56,128
5:0-2560-1	2,560	25.8	640	1,280	DAPC	640	18,208	720	50,368

Table S1: Table listing all the simulations run. Each simulation was 10 μs long, making a total of 0.3 ms of coarse-grained simulation. The saturated lipids DLPC, DPPC and DAPC correspond to the coarse-grained lipids PC 3:0, PC 4:0 and PC 5:0 respectively. The id of each simulation is based on the number of beads in the tails of the saturated lipid, the number of lipids in the bilayer and the repeat number. All simulations have unsaturated lipids, saturated lipids and cholesterol in the same relative 3:5:2 composition, with the exceptions of 5:0-2880-1 (3:5:1) and 5:0-2560-1 (2:4:2). All simulations were run at 310K, with the exception of 3:0-6000-4 which was run at 323 K. Since all the molecules were described using the MARTINI coarse-grained forcefield, each bead represents approximately four atoms (excluding hydrogen). A single water bead therefore represents four water molecules. Since a sodium or chloride bead contains the first hydration shell this also contains six water molecules, ensuring that, with the exception of the 6,000 lipid simulations, there are ~30 waters per phospholipid, thereby ensuring the bilayers are above the swelling limit. Additional water beads were added to the 6 000 lipid simulations in case longer wavelength fluctuations occurred.

For each leaflet separately (upper and lower):

A Cholesterol Unsaturated Saturated — = difference

densities

interface_mask edges regions

U S

B

Phosphate

density cubic interpolation of z-values surface
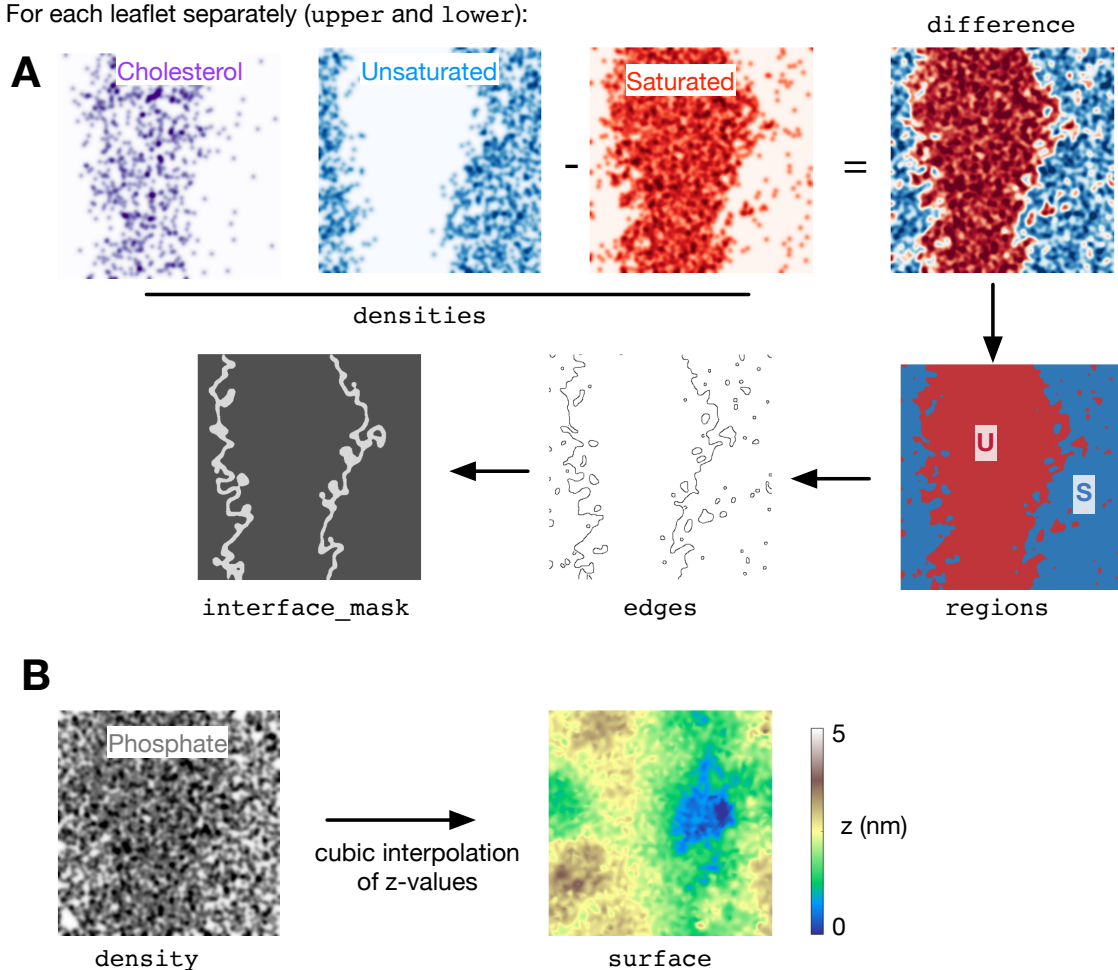
5

z (nm)

0

Figure S1: Schematic illustrating how each leaflet of the bilayer in each frame of every simulation is analysed. (A) First the planar positions of the lipids (as defined by the (x, y) coordinates of the phosphate (PO4) or hydroxyl (ROH) beads) are convolved with a Gaussian of width 0.8 nm to create density arrays. Subtracting the saturated density from the unsaturated density yields a difference array. Defining any region where the saturated density is higher (i.e. difference > 0) yields a simple regions array. Applying the Canny edge detection algorithm found in the python scikit.images module creates an array of edges. Finally convolving this with a Gaussian, again of width 0.8 nm, then subtracting from unity and only keeping those interfaces where the area is $> 1\%$ of the total area produces an array defining the main interfaces (interface_mask). (B) We only use the phospholipids to define the surface of the leaflet since cholesterol tends to sit lower in the bilayer. An array of the z values of the phosphate beads is (cubically) interpolated onto a grid of width 0.1 nm. To avoid a convex hull the array is first duplicated in the x, y directions. This yields a surface array that describes topology of the leaflet being considered.
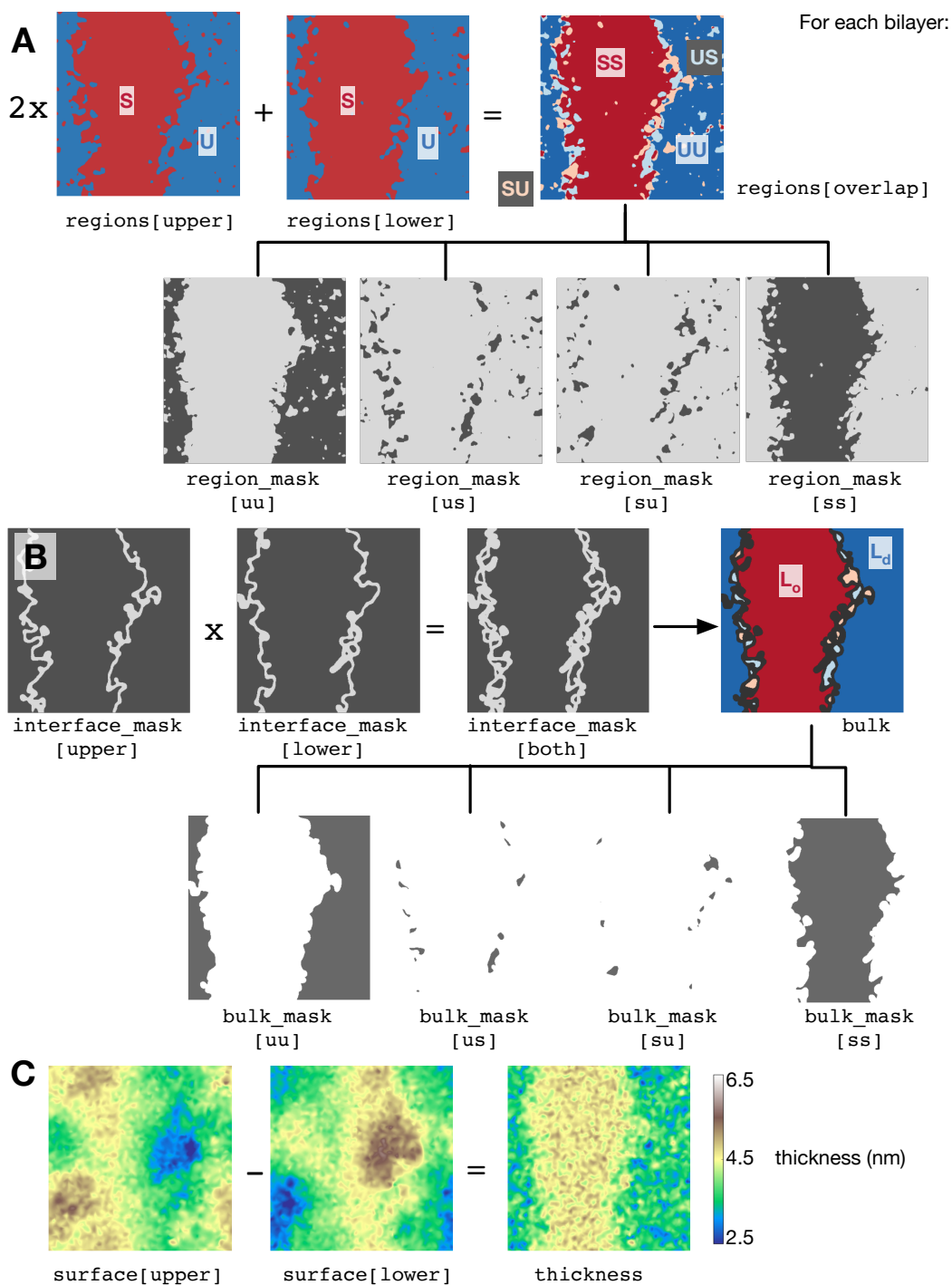
Figure S2: Schematic illustrating how each bilayer in each frame of every simulation is analysed. (A) The `regions` arrays of both leaflets are combined as shown to yield at array, called `regions[overlap]`, that shows the spatial distribution of each of the four distinct lipid arrangements (the registered regions: SS, UU and the antiregistered regions: SU, US). Each of these can be extracted making a mask (called `region_mask`) that can be multiplied by other arrays (such as `density` or `thickness`) to calculate various properties of that set of fine-grained regions. (B) If instead we are concerned about the *bulk* leaflet composition of different phases we need to exclude the interface regions and define each contiguous region by the dominant lipid arrangement. We begin by multiplying the `interface_mask` arrays for each leaflet and then, again using the `scikit-image` python module, identifying all the contiguous regions. These are assigned to a bulk phase according to their dominant composition, creating the `bulk` array. Again, masks can be extracted from this array which can be multiplied by other arrays to determine different properties, such as the lipid composition, of these phases. (C) Lastly, simply subtracting the two `surface` arrays gives an array of the bilayer `thickness`.
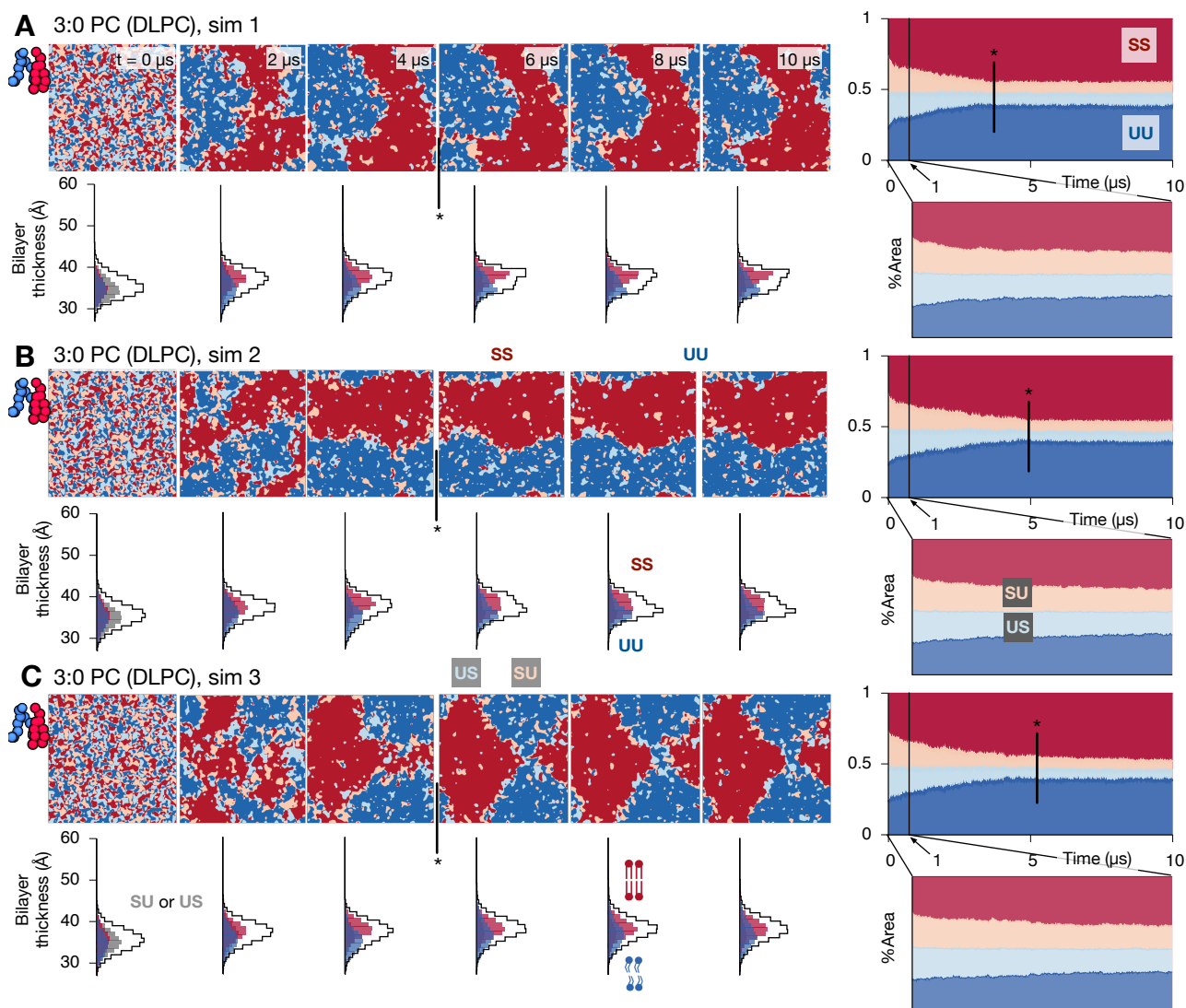
Figure S3: Using DLPC (3:0 PC) leads to a small amount of hydrophobic mismatch compared to the unsaturated lipid, DLiPC, and promotes the formation of registered domains. Images showing the arrangement of lipids in both leaflets for (A) sim1, (B) sim2 and (C) sim3. There are four possible arrangements: both leaflets saturated (SS, red), both unsaturated (UU, blue), or asymmetric arrangements (SU, pink or US, light blue). To the right of the snapshots is plotted how the area of each region varies with time, including a pull out showing the behaviour in the first 1 μs, and below are a series of distributions of the thickness of the bilayer, showing that there is a small difference in thickness between the ordered and disordered regions. Note that the large ordered region becomes gel-like around 4-5 μs in each of the three simulations. The transition is marked with an asterisk. These simulations were run at 310 K; to verify that the overall behaviour is not significantly affected a simulation was run at 323 K and analysed (Fig. S4).

A 3:0 PC (DLPC), sim1 @ 37 °C
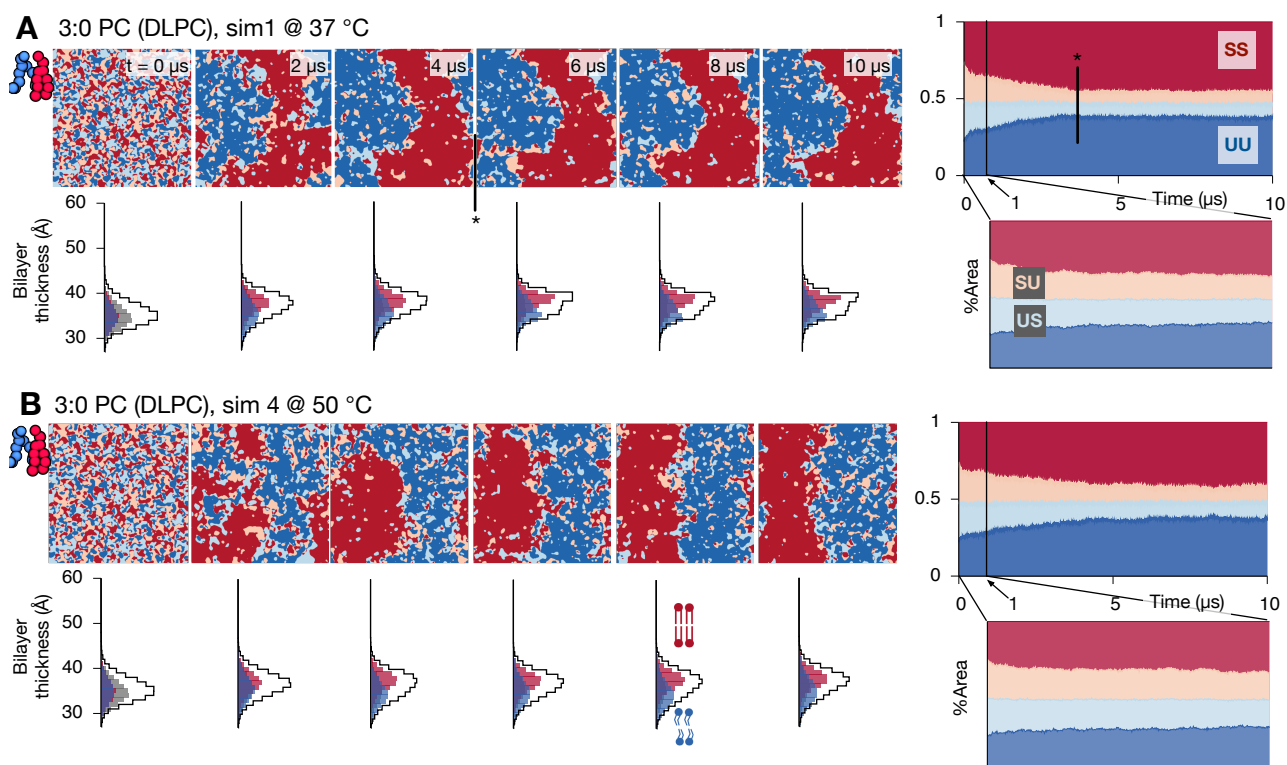
B 3:0 PC (DLPC), sim 4 @ 50 °C

Figure S4: Repeating a DLPC (3:0 PC) simulation at a higher temperature does not significantly alter the phase separation kinetics. (A) For comparison one of the 310 K simulation is shown. (B) The higher temperature prevents the registered ordered region becoming gel-like. As before, there is little thickness difference between the registered domains.
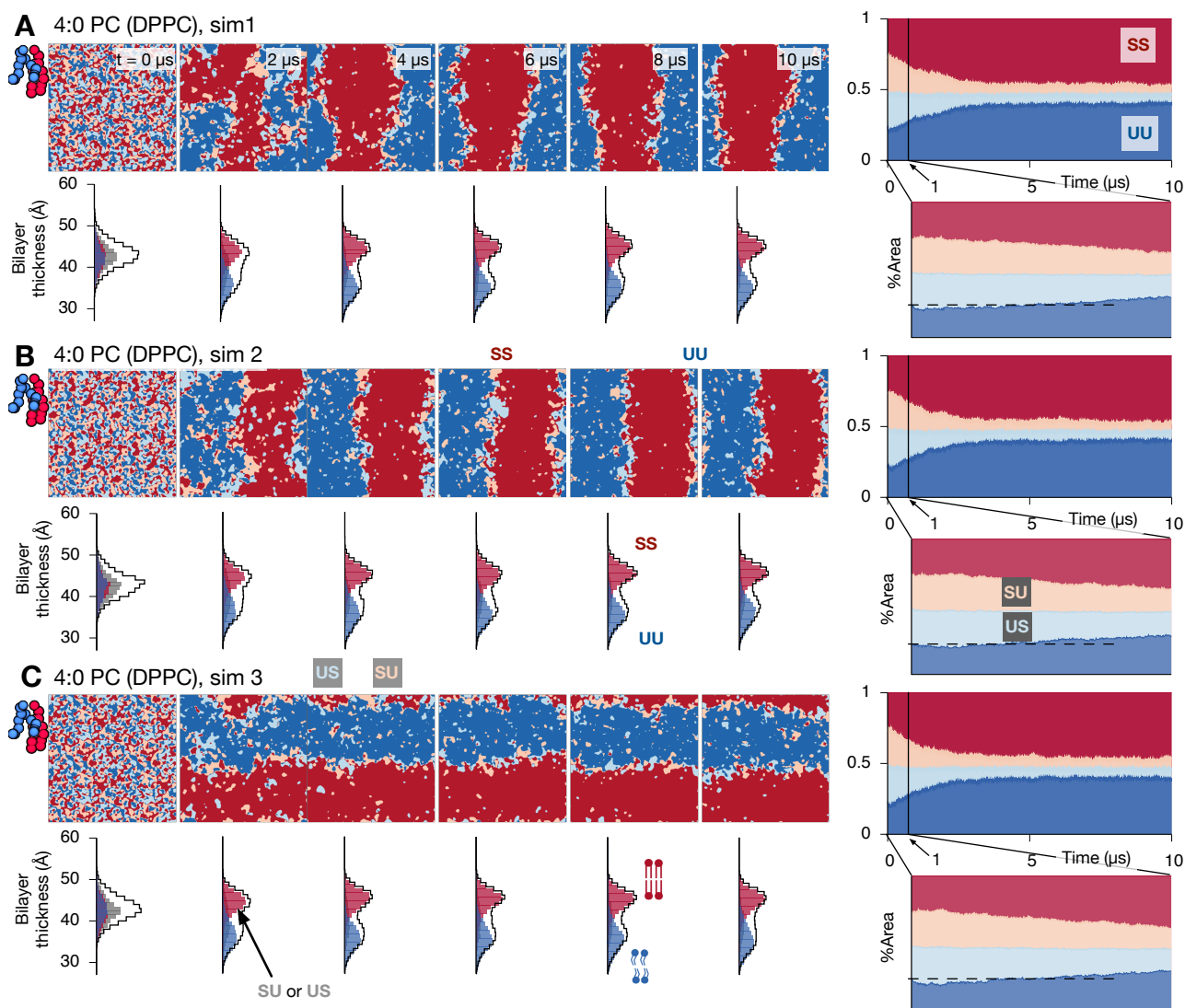
Figure S5: Using DPPC (4:0 PC) creates a moderate amount of hydrophobic mismatch with the unsaturated lipid, DLiPC, leading to a very short period where the antiregistered domains grow before the registered domains begin to dominate. Images showing the arrangement of lipids in both leaflets for (A) sim1, (B) sim2 and (C) sim3. There are four possible arrangements: both leaflets saturated (SS, red), both unsaturated (UU, blue), or asymmetric arrangements (SU, pink or US, light blue). To the right of the snapshots is plotted how the area of each region varies with time, including a pull out showing the behaviour in the first 1 μs, and below are a series of distributions of the thickness of the bilayer, showing that there is a moderate difference in thickness between the ordered and disordered regions.
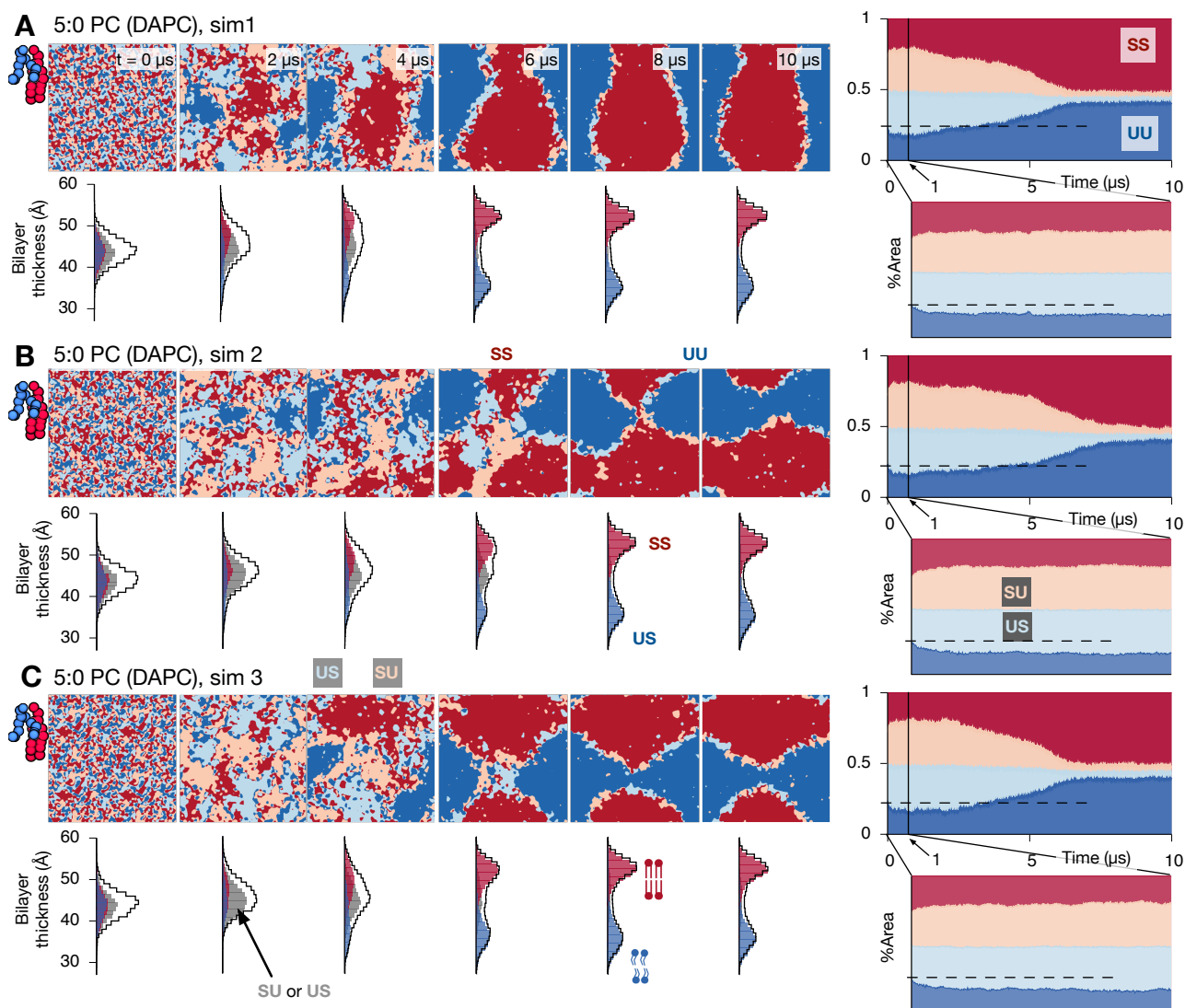
S7

Figure S6: Using DAPC (5:0 PC) creates a large amount of hydrophobic mismatch with the unsaturated lipid, DLiPC, leading to a prolonged period where the antiregistered domains dominate before the registered domains begin to grow. Images showing the arrangement of lipids in both leaflets for (A) sim1, (B) sim2 and (C) sim3. There are four possible arrangements: both leaflets saturated (SS, red), both unsaturated (UU, blue), or asymmetric arrangements (SU, pink or US, light blue). To the right of the snapshots is plotted how the area of each region varies with time, including a pull out showing the behaviour in the first 1 μs, and below are a series of distributions of the thickness of the bilayer, showing that there is a large difference in thickness between the ordered and disordered regions.
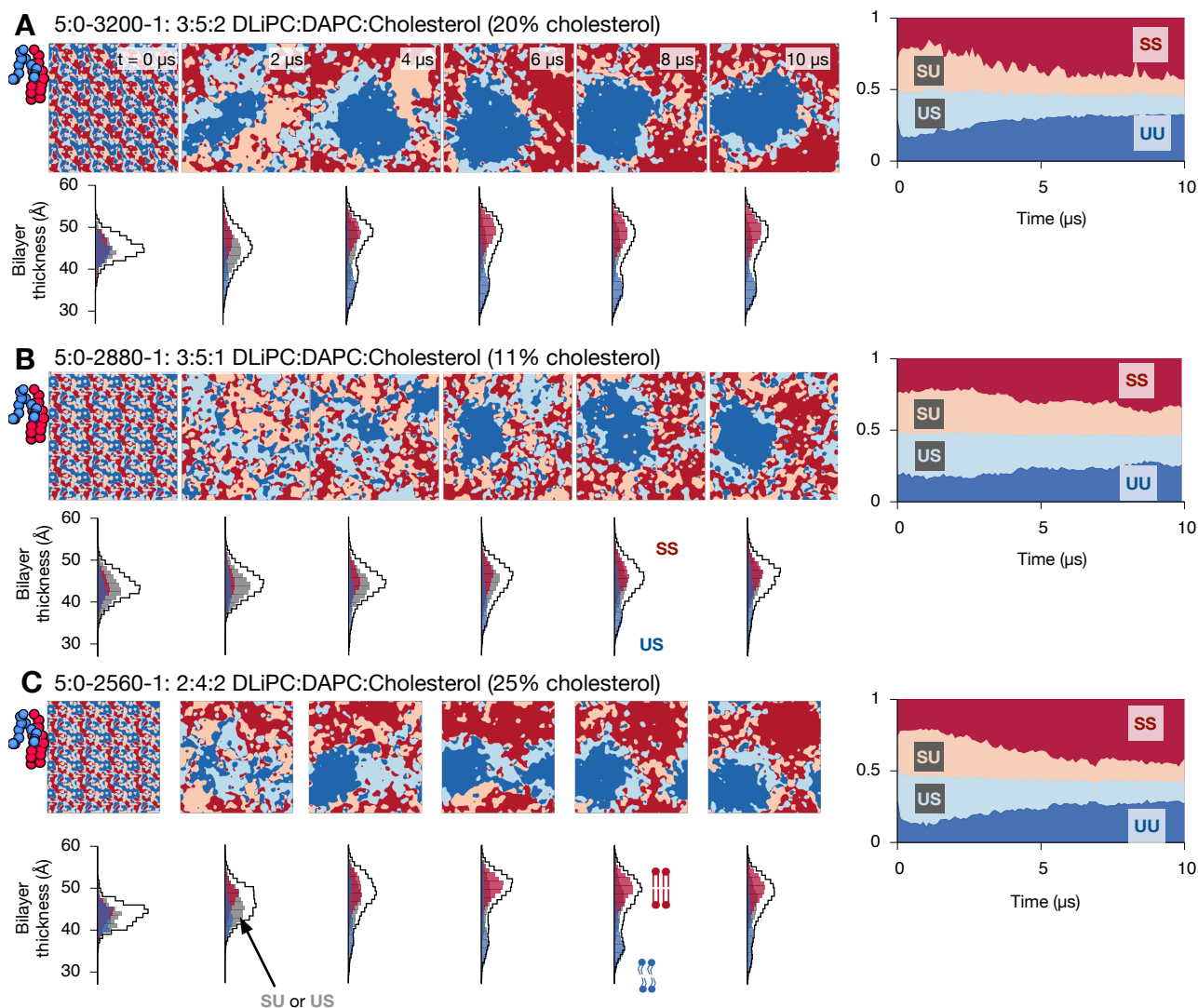
Figure S7: Compositions with different cholesterol fractions also show two-step kinetics. All three simulations used DAPC (5:0 PC) to create a large hydrophobic mismatch with the unsaturated lipid, DLiPC. (A) Our standard 3:5:2 DLiPC:DAPC:Cholesterol composition shows two-step kinetics in a 3,200 lipid patch (as in the main 6,000 lipid simulations). (B) Reducing (11%) or (C) increasing (25%) the proportion of cholesterol quantitatively alters the kinetics, but in all cases there is an initial period where the antiregistered domains grow, before the registered domains begin to dominate. Since the composition was altered by deleting lipids, both (B) and (C) have slightly fewer lipids than (A) and are consequently slightly smaller. The repeating pattern at t=0 clearly shows how each patch was created by tessellating a smaller patch, as described in the Methods.
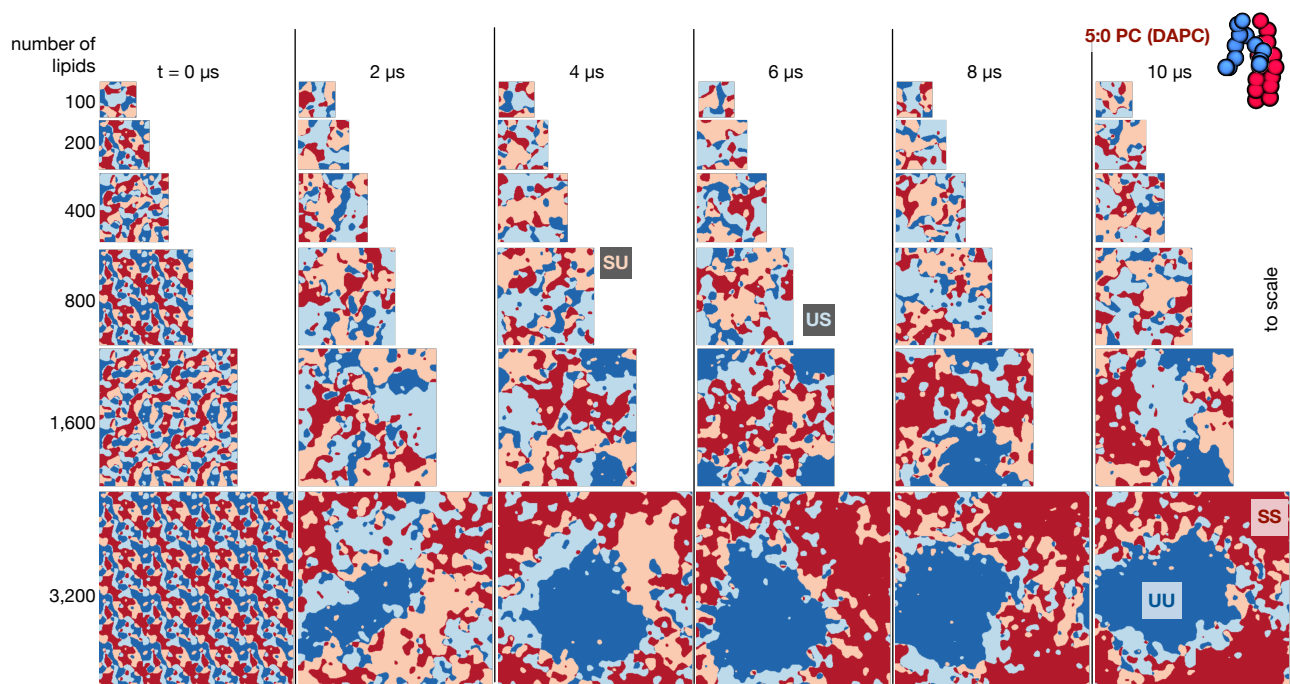
Figure S8: Decreasing the size of the membrane patch inhibits the formation of the registered domains. Shown here to scale are plane views of a series of simulations where the number of lipids is varied from 100 to 3,200. All have the same composition of 3:5:2 DLiPC:DAPC (5:0 PC): cholesterol. For comparison all the simulations in Fig. 2 and Fig. S3, S4, S5 & S6. contain 6,000 lipids.
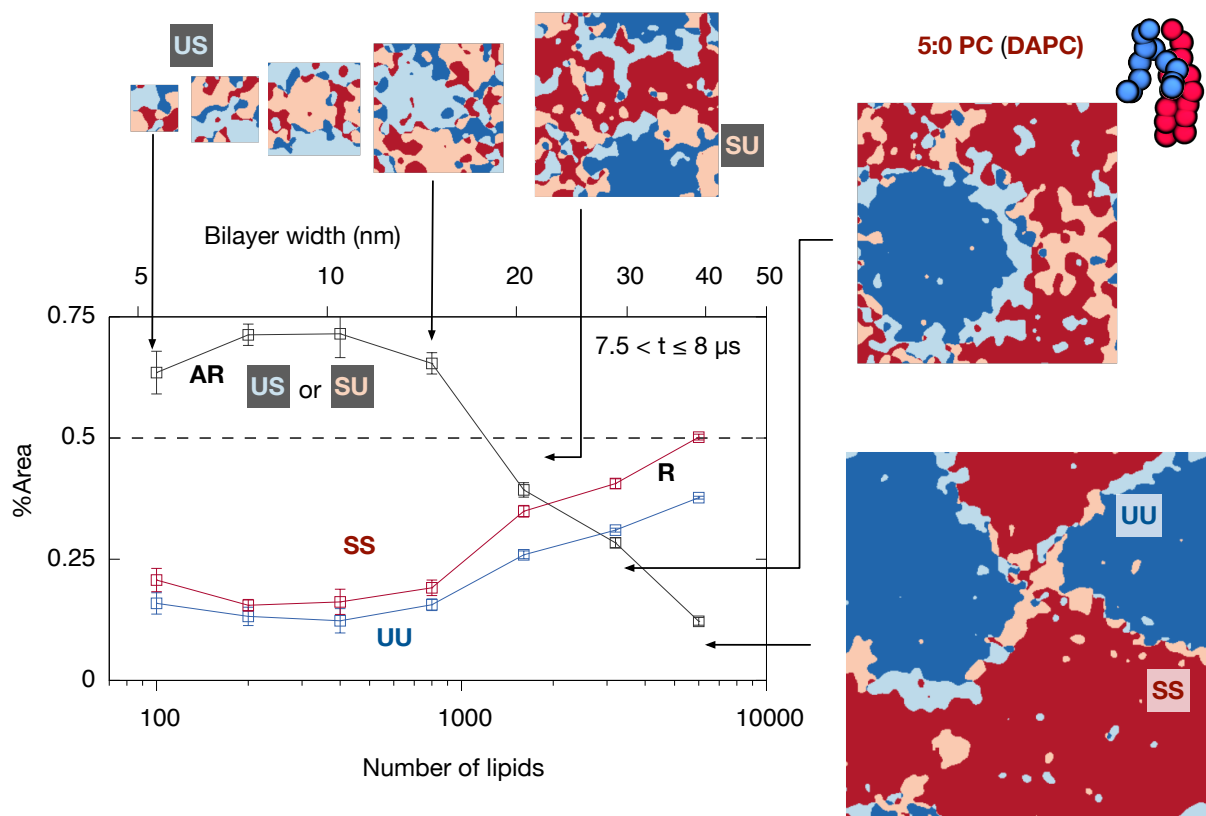
Figure S9: The prolongation of the antiregistered domains by decreasing the size is not a time-dependent effect. A series of simulations of the 5:0 lipid (3:5:2 DLiPC:DAPC:cholesterol) of different sizes. Since the periodic boundary conditions are imposed, this limits the maximum lengthscale in each simulation. After 8 μs, simulations with $\leq$ 800 lipids (size $\leq$ 14.9 nm) remain dominated by antiregistered domains whereas the simulation within 6,000 lipids (size = 39.6 nm) has separated into ordered and disordered registered domains. (This is the same simulation as in Fig. 2C). The two simulations with 1,600 and 3,200 lipids show intermediate behaviour with varying proportions of antiregistered and registered domains. Areas averaged over the time period $7.5 < t \leq 8.0$ μs of each simulation.
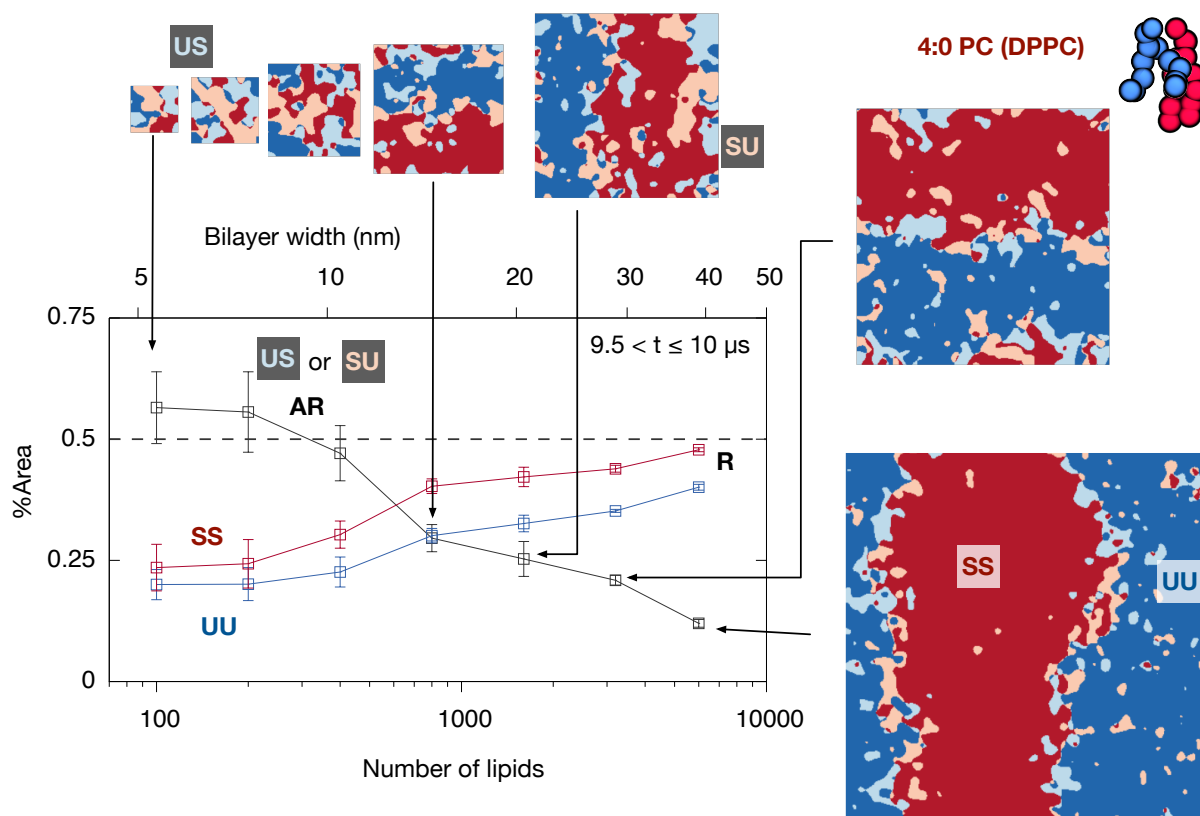
Figure S10: Decreasing the saturated tails to 4 beads reduces the simulation size required to promote antiregistration. A series of simulations of the 4:0 saturated lipid (3:5:2 DLiPC:DPPC:cholesterol) of different sizes. Since the periodic boundary conditions are imposed, this limits the maximum lengthscale in each simulation. Simulations with ≤ 400 lipids (size ≤ 10.9 nm) show only a slight preference for antiregistration (i.e., a $> 50\%$ AR area). Relative to Fig. S9, the finite-size effect is very weak and, as would be expected for smaller hydrophobic mismatch, occurs at a smaller lengthscale. Areas averaged over the time period $9.5 < t \leq 10.0$ μs of each simulation.
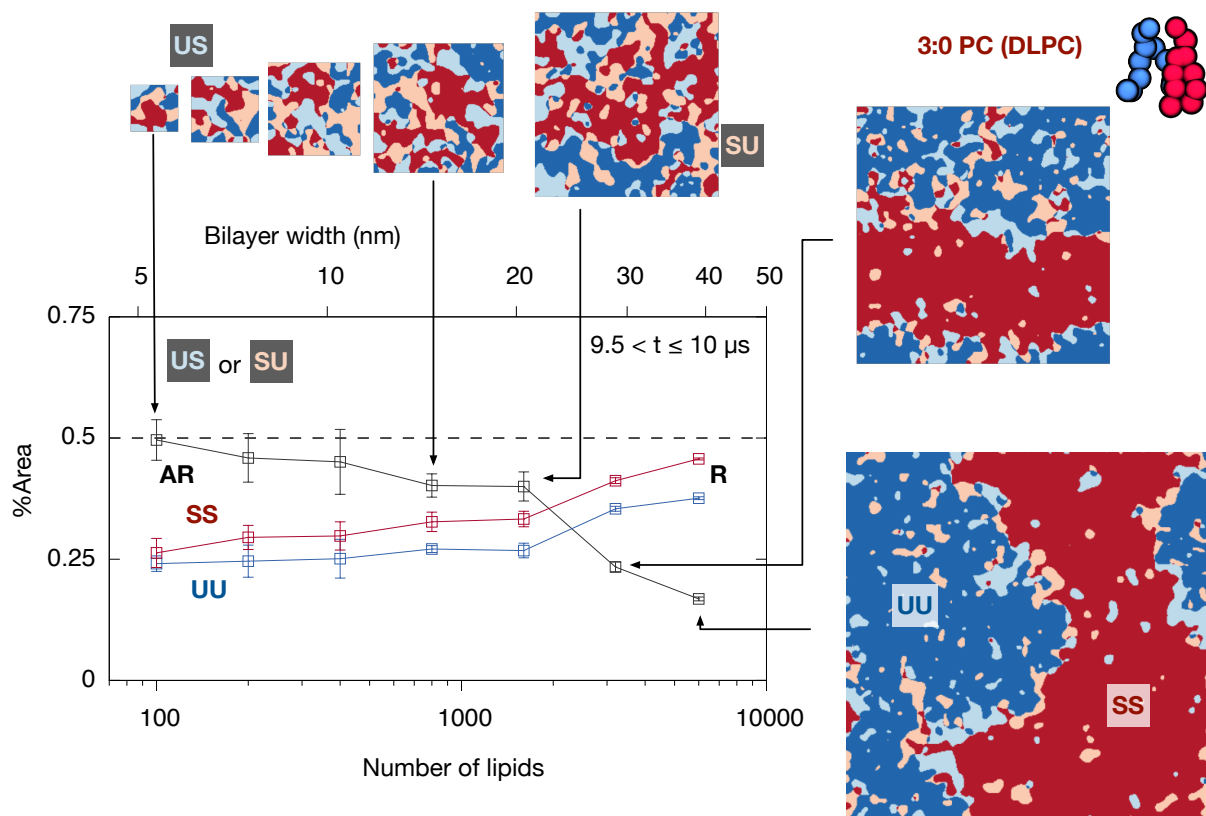
Figure S11:   Simulations with the 3:0 saturated lipid do not show a resolvable preference for antiregistration at any simulation size. A series of simulations of the 3:0 lipid (3:5:2 DLiPC:DLPC:cholesterol) of different sizes. Since the periodic boundary conditions are imposed, this limits the maximum lengthscale in each simulation. However, in contrast to Fig. S9, there is no sign of the AR area exceeding 50 %, which would indicate a preference for antiregistration. It is possible that the significant impurity of the phases in this system tends to bring the measurement closer toward the high-temperature limit of uncorrelated leaflets (for which 50 % AR area is expected [1]). Areas averaged over the time period $9.5 < t \leq 10.0\,\mu$s of each simulation.
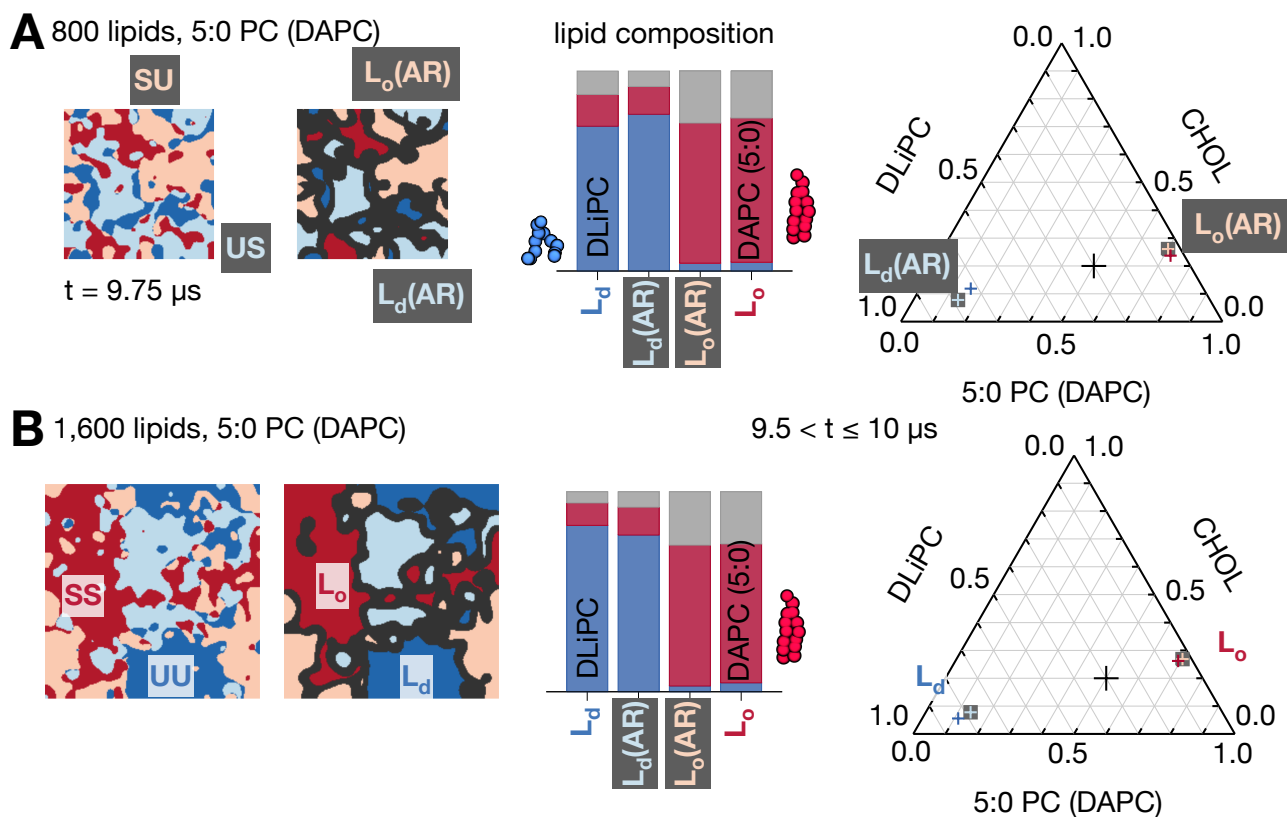
Figure S12: To measure the compositions of the bulk antiregistered phases in the DAPC system, one can use small simulations to inhibit registered phase formation (in the main text we analysed the large simulations but at intermediate times when significant antiregistered phases existed). Here we perform the same analysis as used on the large system in Fig. 4, but applied to smaller systems. In the 800 lipid simulation (A) there is very little registered phase present, while in the 1,600 lipid simulation (B) there is a similar proportion of registered and antiregistered phases (cf. Fig. 3). Both yield similar leaflet composition measurements for the bulk antiregistered phases.
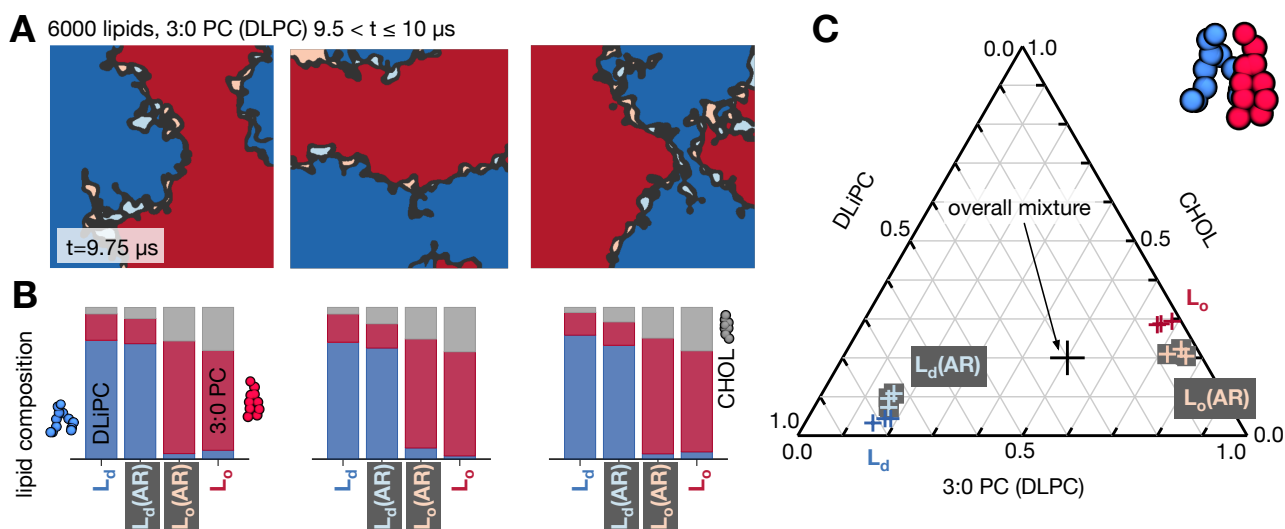
Figure S13: The phase compositions of the DLPC (3:0 PC) simulations at late time are determined as described in the Methods. (A) Plane views of each of the three simulations, coloured by the phases present. (B) The lipid composition averaged over the last 0.5 μs of each simulation is plotted for each of the four phases. (C) These compositions are also plotted on a Gibbs triangle.

Figure S14: The phase compositions of the DPPC (4:0 PC) simulations at late time are determined as described in the Methods. (A) Plane views of each of the three simulations, coloured by the phases present. (B) The lipid composition averaged over the last 0.5 μs of each simulation is plotted for each of the four phases. (C) These compositions are also plotted on a Gibbs triangle.
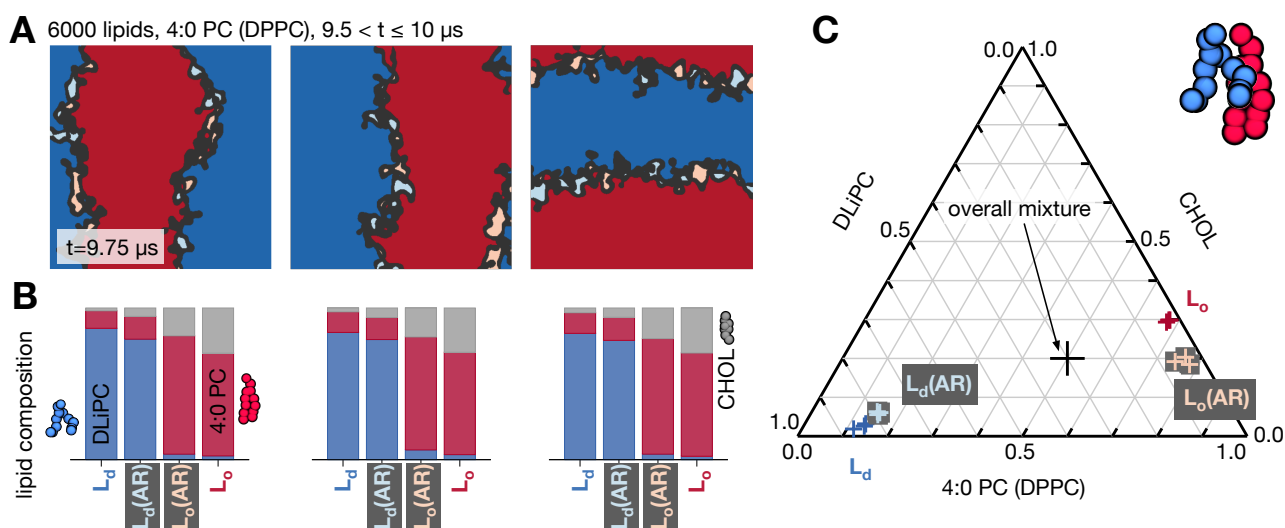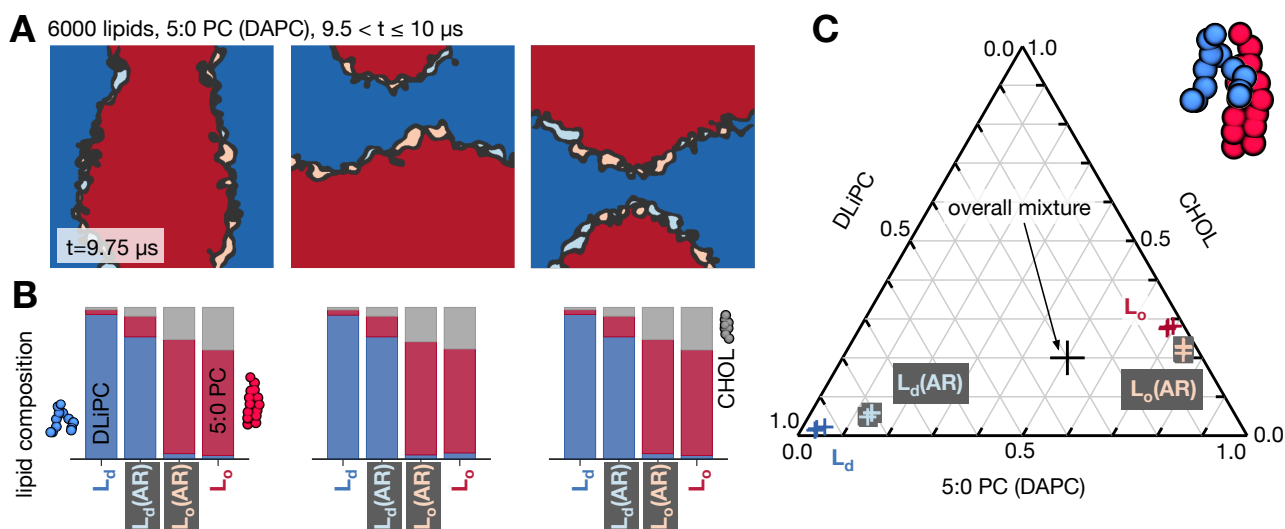
Figure S15: The phase compositions of the DAPC (5:0 PC) simulations at late time are determined as described in the Methods. (A) Plane views of each of the three simulations, coloured by the phases present. (B) The lipid composition averaged over the last 0.5 μs of each simulation is plotted for each of the four phases. (C) These compositions are also plotted on a Gibbs triangle.

Figure S16: The leaflet phase compositions of the DAPC (5:0 PC) simulations at intermediate time is determined as described in the Methods. (A) Plane views of each of the three simulations, coloured by the phases present. (B) The lipid composition averaged over the intermediate period 4.5-5 μs of each simulation is plotted for each of the four phases. (C) These compositions are also plotted on a Gibbs triangle.

Semi-microscopic model
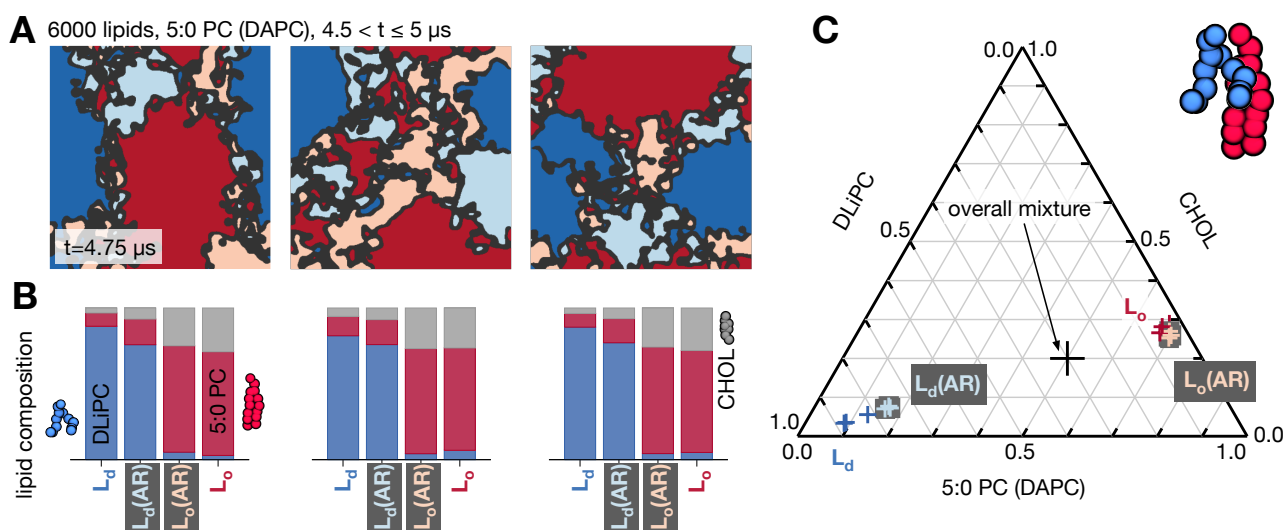
Extensive discussion of the semi-microscopic theoretical model used to derive the leaflet-leaflet free energy $f(\phi^{\mathrm{t}}, \phi^{\mathrm{b}})$ is given in Ref. 2 and in Refs. 1, 3. Here we qualitatively outline the key ideas to provide further context for the Introduction and Theory sections of the main text.

As mentioned in the main text, the model describes a lipid bilayer patch as a lattice comprising two apposed leaflets. The top and bottom leaflets of each lattice site are occupied by one of two model species S and U. As well as the species, we keep track of variables describing each lipid's hydrophobic tail length. The lattice Hamiltonian is

$$
\begin{aligned}
H = \sum_{<i,j>} \left(V_{\hat{\phi}_i^{\mathrm{t}} \hat{\phi}_j^{\mathrm{t}}} + V_{\hat{\phi}_i^{\mathrm{b}} \hat{\phi}_j^{\mathrm{b}}} \right) + \sum_{<i,j>} \tfrac{1}{2} \tilde{J} (d_i - d_j)^2 \\
+ \sum_i \tfrac{1}{2} B (\Delta_i)^2 + \sum_i \tfrac{1}{2} \kappa \left((\ell_i^{\mathrm{t}} - \ell_0^{\mathrm{t}i})^2 + (\ell_i^{\mathrm{b}} - \ell_0^{\mathrm{b}i})^2 \right) ,
\end{aligned}
\tag{S1}
$$

where $\hat{\phi}_i^{\mathrm{t(b)}} = 1$ if the top (bottom) leaflet at site i contains an S amphiphile, $\hat{\phi}_i^{\mathrm{t(b)}} = 0$ if U. The total bilayer thickness of a given site is $d_i = \ell_i^{\mathrm{t}} + \ell_i^{\mathrm{b}}$ and the leaflet thickness difference is $\Delta_i = \ell_i^{\mathrm{t}} - \ell_i^{\mathrm{b}}$. Species-dependent ideal hydrophobic lengths are $\ell_0^{\mathrm{t(b)}i} = \ell_{S0}$ for an S amphiphile at the top (bottom) of site i, or ℓ_{U0} for U. Each site is *pairwise* registered (SS or UU) or antiregistered (SU or US). $\Delta_0 \equiv \ell_{S0} - \ell_{U0}$ reflects both tail length mismatch and, implicitly[4], tail structural mismatch between species.

$V \equiv V_{10} - \tfrac{1}{2}(V_{00} + V_{11})$ is an Ising-like term for intra-leaflet interactions independent of tail length, e.g., between head-groups. It provides a purely intra-leaflet immiscibility interaction as used in phenomenological theories[5–7]. The "direct" coupling B promotes transbilayer symmetry (SS and UU lattice sites) by minimising mismatch across the midplane. The hydrophobic "indirect" coupling $\tilde{J}$ tends to favour asymmetry (SU and US sites) by penalising mismatch in the bilayer thickness profile. However, as well as implicitly coupling the leaflets, the hydrophobic mismatch also contributes to immiscibility and hence to the overall driving force for lateral phase separation (cf. Fig. 5 and Discussion in the main text). This dual role emerges naturally from the model[2] and could not be captured in a theory organised in terms of purely intra- and inter-leaflet free-energy contributions. ($J \equiv 4\tilde{J}$ appears upon a mean-field approximation of Eq. S1[2].) The stretch modulus κ penalises variation from species-dependent ideal length.

Δ_0 works with both J and B to control both the indirect and direct couplings. Hence, varying tail length mismatch alone is approximated by changing J, while varying direct coupling (e.g., tail structure mismatch) is approximated by changing B. The precise mechanisms underlying direct inter-leaflet coupling are not relevant to the model, since B can simply be mapped to an effective value of the (direct) inter-leaflet mismatch energy per area γ, widely estimated in the literature[8–12]:

$$
\gamma = \frac{\Delta_0^2 \kappa B}{2a^2 (\kappa + 2B)}
\tag{S2}
$$

where a is the lattice spacing, roughly the lateral size of a lipid.

We finally sketch out the derivation of $f(\phi^{\mathrm{t}}, \phi^{\mathrm{b}})$, of which details can be found in Ref. 2. Having defined the semi-microscopic model, we first use a mean-field approximation for the neighbour interaction terms[2]. The goal is then to arrive at a free-energy density $f(\phi^{\mathrm{t}}, \phi^{\mathrm{b}})$ as a function of locally averaged composition variables $\phi^{\mathrm{t}}, \phi^{\mathrm{b}}$. These coarse-grained variables constrain the allowed microscopic arrangements (e.g., there cannot be any SU or SS lattice sites in a region where the top leaflet has purely U lipids, $\phi^{\mathrm{t}} \to 0$). Integrating over the allowed arrangements and over the leaflet thickness variables for given $\phi^{\mathrm{t}}, \phi^{\mathrm{b}}$ finally yields a lengthy expression for the free energy $f(\phi^{\mathrm{t}}, \phi^{\mathrm{b}})$[2]. Estimating physically reasonable values[2] for the parameters typically yields a free-energy landscape of the form shown in the main text (Fig. 1B), such that the registered (R) minima are lowest in free energy but (as long as B is not too large) AR minima exist too. To derive phase coexistences, in analogy with the common tangent construction, common tangent *planes* determine phases which are equal in their top-leaflet chemical potential, bottom-leaflet chemical potential, and surface tension[2,7].

To study the competing instability kinetics (Fig. 1C), this bulk free energy $f(\phi^{\mathrm{t}}, \phi^{\mathrm{b}})$ can in turn serve as the "Landau part" of a Ginzburg-Landau linear stability analysis which also incorporates gradient energies arising from the V and $\tilde{J}$ terms of the Hamiltonian. This is briefly described in the main text and shown in detail in Ref. 2.

References

1. Williamson, J. J.; Olmsted, P. D. *Phys. Rev. E* **2015,** *92,* 052721.

2. Williamson, J. J.; Olmsted, P. D. *Biophys. J.* **2015,** *108,* 1963.

3. Williamson, J. J.; Olmsted, P. D. *Soft Matter* **2015,** *11,* 8948.

4. Komura, S.; Shirotori, H.; Olmsted, P. D.; Andelman, D. *Europhys. Lett.* **2004,** *67,* 321.

5. Collins, M. D.; Keller, S. L. *Proc. Natl. Acad. Sci.* **2008,** *105,* 124.

6. Wagner, A. J.; Loew, S.; May, S. *Biophys. J.* **2007,** *93,* 4268.

7. Garbès Putzel, G.; Schick, M. *Biophys. J.* **2008,** *94,* 869.

8. Pantano, D. A.; Moore, P. B.; Klein, M. L.; Discher, D. E. *Soft Matter* **2011,** *7,* 8182.

9. Risselada, H. J.; Marrink, S. J. *Proc. Natl. Acad. Sci.* **2008,** *105,* 17367.

10. May, S. *Soft Matter* **2009,** *5,* 3148.

11. Garbès Putzel, G.; Uline, M. J.; Szleifer, I.; Schick, M. *Biophys. J.* **2011,** *100,* 996.

12. Blosser, M. C.; Honerkamp-Smith, A. R.; Han, T.; Haataja, M.; Keller, S. *Biophys. J.* **2015,** *109,* 2317.